

# Defect characterization and charge transport measurements in high-resolution Ni/n-4H-SiC Schottky barrier radiation detectors fabricated on 250 $\mu\text{m}$ epitaxial layers

Cite as: J. Appl. Phys. 129, 244501 (2021); doi: 10.1063/5.0049218

Submitted: 2 March 2021 · Accepted: 9 June 2021 ·

Published Online: 25 June 2021



Joshua W. Kleppinger, Sandeep K. Chaudhuri, OmerFaruk Karadavut, and Krishna C. Mandal<sup>a)</sup>

## AFFILIATIONS

Department of Electrical Engineering, University of South Carolina, Columbia, South Carolina 29208, USA

<sup>a)</sup>Author to whom correspondence should be addressed: mandalk@cec.sc.edu. Tel.: +1 (803) 777-2722

## ABSTRACT

Advances in the growth processes of 4H-SiC epitaxial layers have led to the continued expansion of epilayer thickness, allowing for the detection of more penetrative radioactive particles. We report the fabrication and characterization of high-resolution Schottky barrier radiation detectors on 250  $\mu\text{m}$  thick n-type 4H-SiC epitaxial layers, the highest reported thickness to date. Several  $8 \times 8 \text{ mm}^2$  detectors were fabricated from a diced 100 mm diameter 4H-SiC epitaxial wafer grown on a conductive 4H-SiC substrate with a mean micropipe density of  $0.11 \text{ cm}^{-2}$ . From the Mott-Schottky plots, the effective doping concentration was found to be in the range  $(0.95\text{--}1.85) \times 10^{14} \text{ cm}^{-3}$ , implying that full depletion could be achieved at  $\sim 5.7 \text{ kV}$  ( $0.5 \text{ MV/cm}$  at the interface). The current-voltage characteristics demonstrated consistently low leakage current densities of  $1\text{--}3 \text{ nA/cm}^2$  at a reverse bias of  $-800 \text{ V}$ . This resulted in the pulse-height spectra generated using a  $^{241}\text{Am}$  alpha source (5486 keV) manifesting an energy resolution of less than 0.5% full width at half maximum (FWHM) for all the detectors at  $-200 \text{ V}$ . The charge collection efficiencies (CCEs) were measured to be 98–99% with no discernable correlation to the energy resolution. A drift-diffusion model fit to the variation of CCE as a function of bias voltage, revealed a minority carrier diffusion length of  $\sim 10 \mu\text{m}$ . Deep level transient spectroscopy measurements on the best resolution detector revealed that the excellent performance was the result of having ultralow concentrations of the order of  $10^{11} \text{ cm}^{-3}$  lifetime limiting defects— $\text{Z}_{1/2}$  and  $\text{EH}_{6/7}$ .

Published under an exclusive license by AIP Publishing. <https://doi.org/10.1063/5.0049218>

## I. INTRODUCTION

4H-silicon carbide (SiC) semiconductor devices have established themselves for harsh environment applications such as high radiation fields and high temperature zones, due to the unique combination of physical properties such as high average displacement threshold energy, high bandgap, and high thermal conductivity.<sup>1–4</sup> 4H-SiC is also well suited for optical component power system applications due to its high optical damage threshold.<sup>5</sup> Additionally, 4H-SiC has excellent charge transport properties, which is a pre-requisite for efficient charge collection, fast readout, and high timing and pulse-height resolution of semiconductor radiation detectors.<sup>6–8</sup>

Schottky barrier diodes (SBD) fabricated on 4H-SiC epitaxial layers have hence established themselves as high-resolution radiation detectors.<sup>9–13</sup> Owing to its wide bandgap of 3.27 eV and high

thermal conductivity of  $4.9 \text{ W/cm}^2$ , 4H-SiC Schottky barrier detectors can operate at temperatures well above room temperature. In fact, SiC devices can operate continuously at  $1000^\circ\text{C}$  without any considerable alteration in the detection properties.<sup>14</sup> In addition, because of the wide bandgap, SiC detectors are practically blind to visible light and hence do not need light-tight arrangements for radiation detection purpose. Furthermore, as has been mentioned above, it is a radiation hard material due to the high threshold displacement energies of the constituent elements (19 eV for C and 42 eV for Si).<sup>15</sup> SiC Schottky barrier detectors can provide 100% charge collection efficiency, which enables them to make precise measurements of ionizing radiation dose and intensity.<sup>16</sup> 4H-SiC detectors have also exhibited excellent timing properties with a demonstrated timing resolution as high as 117 ps.<sup>17</sup> The unique combination of such physical properties makes 4H-SiC detectors

find applications in the field of cutting-edge high-energy physics experiments such as real-time diagnosis of laser-accelerated particle beams generating plasma environments<sup>18</sup> and direct detection of sub-GeV dark matter<sup>19</sup> in addition to the main-stream radiation detection. Altogether, this makes epitaxial 4H-SiC SBDs advantageous for energy and security applications such as *in situ* nuclear waste characterization or monitoring of the nuclear core reactor, space missions, and high-energy physics applications such as laser-generated plasma radiation detection or synchrotron radiation detection.<sup>18,20,21</sup>

4H-SiC SBDs fabricated on thin (20  $\mu\text{m}$ ) epilayers is a proven technology for charged particle detection achieving resolutions as high as 0.25% full width half maximum (FWHM) for 5486 keV alpha particles.<sup>22,23</sup> In terms of  $x/\gamma$ -photon adsorption, 4H-SiC SBDs are reported to be sensitive to x rays up to 59.6 keV in epilayers with an active thickness as low as 16  $\mu\text{m}$ .<sup>24–27</sup> The resolution is reported to improve with increased epilayer thickness with a resolution as high as 2.1% for 59.5 keV gamma rays achieved with fully depleted 124  $\mu\text{m}$  detectors.<sup>11</sup> Our previous studies on x-ray sensitivity of SBD detectors, fabricated on 50  $\mu\text{m}$  thick 4H-SiC epitaxial layer, revealed that sensitivity to x rays with energy higher than 3 keV was limited by the active volume thickness.<sup>27,28</sup> Furthermore, the sensitivity to neutron pulses is demonstrated to improve by as much as 139.8% with increased epilayer thickness from 20 to 120  $\mu\text{m}$ .<sup>20</sup> Currently available thick semi-insulating bulk 4H-SiC exhibits large concentration of trapping centers and hence cannot be used as an alternative to epitaxial 4H-SiC for radiation detection.<sup>29–31</sup> Altogether, there is a strong urge for developing radiation detectors on epilayers as thick as possible. However, full depletion of thick epilayers requires bias voltages of several kV, which can lead to the detector breaking down long before reaching the needed bias even with 4H-SiC's high breakdown field of 2 MV/cm. Furthermore, at this high reverse bias, leakage currents could generate too much noise to resolve radiation emission of different energies from radioactive decay events.

In this work, we report the fabrication and characterization of several SBDs fabricated on 250  $\mu\text{m}$  4H-SiC epitaxial layers, which are, incidentally the thickest epilayer detector ever reported for radiation detection. The parent 100 mm diameter wafer had a mean micropipe density of 0.11  $\text{cm}^{-2}$ . Micropipes are thought to be a significant source of premature breakdown and device failure in 4H-SiC substrates.<sup>32–34</sup> With ultralow micropipe concentrations, the performance of the SBDs is expected to be predominantly limited by deep levels within the epitaxial layer. The Schottky barrier detectors were evaluated in terms of its junction behavior via standard current-voltage ( $I$ - $V$ ) and capacitance-voltage ( $C$ - $V$ ) measurements. The radiation detection performance was evaluated using pulse-height spectroscopy (PHS) with an <sup>241</sup>Am alpha source. Capacitance mode deep level transient spectroscopy (DLTS) was applied to characterize traps within the depletion region that might limit the performance of the detectors.

## II. EXPERIMENTAL DETAILS

### A. Detector fabrication

The 250  $\mu\text{m}$  thick n-type 4H-SiC epitaxial layer was grown by hot wall chemical vapor deposition (CVD) on the (0001) face

of a 100 mm diameter, 350  $\mu\text{m}$  thick 4H-SiC conductive substrate (0.015–0.028  $\Omega\text{cm}$ ) with a mean micropipe density (MPD) of 0.11  $\text{cm}^{-2}$ . The substrates were off-cut by  $8^\circ$  toward the  $\langle 11\bar{2}0 \rangle$  direction to minimize the formation of surface defects. The wafer was then diced into  $8 \times 8 \text{ mm}^2$  detector substrates, which were cleaned using a modified recipe to the Radio Corporation of America (RCA) method.<sup>35</sup> To remove any native oxides, the substrates were dipped in concentrated hydrofluoric acid prior to metal contact deposition. Three Schottky barrier detectors (SBD) labeled S1, S2, and S3 were fabricated in a vertical geometry by depositing 10 nm thin Ni circular Schottky contacts on the epilayers using a Quorum Q150T DC sputtering unit at room temperature. The contact diameter was 3.9 mm for S1 and S2 and 2.9 mm for S3. Ni contacts are used for their high metal work function ( $\Phi_M \sim 5 \text{ eV}$ ) and low atomic number compared to other metal contacts with high work function, which are necessary to minimize junction leakage current and charge loss in the metal contact, respectively. Thin nickel contacts are also important to achieve high-energy resolution by minimizing the scattering of incident radiation, especially charged particle, at the window. The Ohmic bottom contact was 100 nm thick Ni with a  $6 \times 6 \text{ mm}^2$  area for all three detectors. A schematic of the detector structure is shown in Fig. 1.

### B. Detector characterization

The junction and depletion properties of the Schottky barrier were characterized by  $I$ - $V$  and  $C$ - $V$  measurements. For  $I$ - $V$

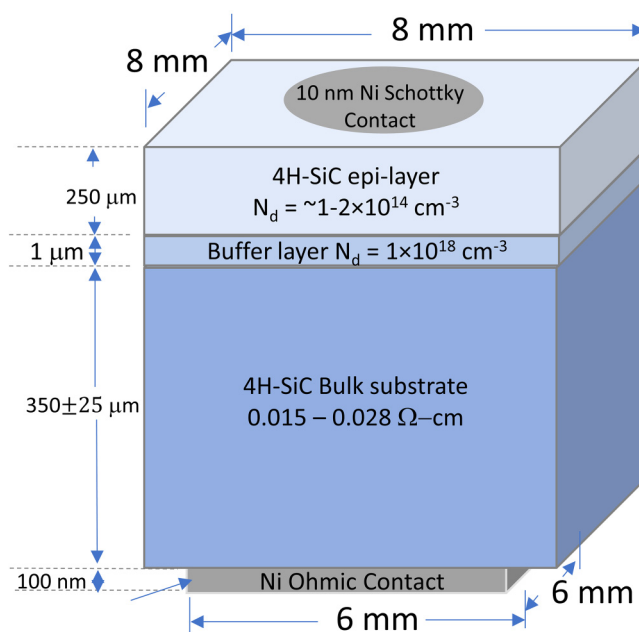


**FIG. 1.** Schematic of the device structure of a Ni/n-4H-SiC radiation detector fabricated on 250  $\mu\text{m}$  epitaxial layers. The  $10^{18} \text{ cm}^{-3}$  buffer layer is in place to reduce the dislocation density in the epilayer.

measurements, the detector was mounted in an electromagnetic interference (EMI) shielded electronic box connected to a Keithley 237 source-measure unit via a low noise triaxial cable. The  $C$ - $V$  measurements were taken using the 1 MHz capacitance meter built into a SULA DDS-12 deep level transient spectroscopy (DLTS) system with the detector mounted in a Janis VPF 800 LN<sub>2</sub> cryostat. Due to the very low thickness of the Ni Schottky contact, the electrical contact between the detector and the tungsten micro-probes in the cryostat could be unreliable even with slightest physical disturbance. To make the electrical connection more rigid and stable, a smaller area ( $\sim 1$  mm diameter)  $\sim 100$  nm thick circular gold contact layer was sputtered overtop the Ni top contact. This is thick enough to survive the sharp tungsten tips, yet of small enough area to not pose any hindrance for the incident radiations during the radiation measurements.

The radiation response was evaluated using a pulse-height spectrometric system consisting of a Cremat CR110 charge-sensitive pre-amplifier, which integrates the input current pulse producing a voltage signal proportional to the total charge induced on the detector electrodes from the ionizing radiation. The output of the CR110 is filtered by an ORTEC 572 shaping amplifier and then sorted into channel numbers by a Canberra Multiport II multichannel analyzer forming a histogram of the frequency of appearance of various pulse heights (incident radiation energies) as a function of pulse-height energy. Such a histogram is commonly referred to as pulse-height spectrum (PHS). The detector mounted on a printed circuit board (PCB) was placed inside an EMI shielded box which was kept under rough vacuum and equipped with a BNC output directly connected to the input of the CR110 pre-amplifier. The spectra were obtained using a  $0.9\ \mu\text{Ci}$   $^{241}\text{Am}$  alpha-particle radio isotopic source emitting primarily three alpha particles of energies 5486, 5443, or 5388 keV. The energy collected by the detector was obtained by calibrating the spectrometric system with a precision pulser. The pulser was fed into the CR110 input through a calibrated feed-through test capacitor (2.46 pF) to generate pulse height spectrum under the measurement conditions identical to the actual PHS acquisition. Knowing the voltage amplitude of the input pulser signal, the material equivalent energy collected is given by

$$E_{\text{pulser}} = \frac{V_{\text{pulser}} \times \epsilon \times C_{\text{test}}}{q}, \quad (1)$$

where  $V_{\text{pulser}}$  is the amplitude of the pulser signal,  $\epsilon$  is the electron-hole pair creation energy, which is taken to be 7.28 eV,<sup>36</sup>  $C_{\text{test}}$  is the capacitance of the test capacitor, and  $q$  is the elementary charge of an electron. Using multiple pulser amplitudes, a linear conversion model can be built between the MCA channel number and the energy collected. The absolute energy resolution for alpha particles with energy  $E_\alpha$  were expressed as either the width (FWHM) of the alpha peaks  $\Delta E$  in the PHS in keV units or in terms of percentage resolution calculated as  $\frac{\Delta E}{E_\alpha} \times 100$ . The charge collection efficiency (CCE) of a detector was obtained as the ratio of the detected energy  $E_\alpha$  to the incident energy of the  $\alpha$  particles (5486 keV).

### C. Deep level transient spectroscopy (DLTS)

DLTS measurements were performed using the SULA DDS-12 DLTS system mentioned in Sec. II B, which consists of a pulse generator for periodic filling of trap levels, a correlator module which uses a modified double boxcar averaging method, and a LabVIEW based data acquisition software. The correlator module allows for up to four initial delay settings allowing four DLTS spectra to be obtained simultaneously in a single temperature scan. The rate window is defined internally as 4.3 times the initial delay. The sample was mounted onto the sample stage in the cryostat and the temperature of the sample was controlled by a Lakeshore LS335 temperature controller. A typical temperature scan ranges from 80 to 790 K. To avoid oxidation of the sample, the cryostat is kept under vacuum for the entire duration of the experiment.

## III. RESULTS AND DISCUSSIONS

### A. Electrical characterization

Figure 2(a) shows the forward bias current-voltage ( $I$ - $V$ ) characteristics of the detectors S1, S2, and S3, which all show rectifying behavior consistent with SBDs. Based on the thermionic emission model of Schottky diodes,<sup>37–39</sup> the forward bias current density  $J_F$  as a function of the applied forward bias  $V_F$  is given by

$$J_F = A^* T^2 \exp\left(-\frac{q\Phi_B}{k_B T}\right) \left[ \exp\left(\frac{qV_F - I_F R_s}{nk_B T}\right) - 1 \right], \quad (2)$$

where  $A^*$  is the effective Richardson constant ( $146\ \text{A}/\text{cm}^2\ \text{T}^2$ ),  $T$  is the absolute temperature of the junction,  $q$  is the elementary charge of an electron,  $\Phi_B$  is the Schottky barrier height,  $k_B$  is Boltzmann's constant,  $R_s$  is the series resistance of the device, and  $n$  is the ideality factor. From the linear fit of  $\ln J_F - V_F$ , the barrier heights of the three detectors were calculated to be 1.35, 1.31, and 1.45 eV for S1, S2, and S3, and the ideality factors were found to be 1.06, 1.00, and 1.08, respectively. Ideality factors slightly greater than 1 suggest that S1 and S3 have minor spatial inhomogeneity of surface barrier height. Figure 2(b) shows the reverse bias characteristics of the detectors. The leakage current densities remained under  $3\ \text{nA}/\text{cm}^2$  up to an applied reverse bias of 800 V for all three detectors. Relative to the mean internal electric field of the space charge region, detector S2 had the lowest leakage current density of  $1\ \text{nA}/\text{cm}^2$  at 100 kV/cm (800 V). At 200 V, the reverse leakage current was of the order of  $0.1\ \text{nA}/\text{cm}^2$  which is comparable to what has been measured only for edge terminated Ni/n-4H-SiC detectors fabricated on  $20\ \mu\text{m}$  thick epilayers.<sup>40</sup>

Figure 3(a) shows the  $C$ - $V$  characteristics for the three detectors given in units of  $\text{pF}/\text{cm}^2$ . For a rectifying metal-semiconductor junction, the relation between capacitance per unit area and applied bias can be expressed as

$$\frac{1}{C^2} = \frac{2}{q\epsilon N_{\text{eff}}} (V_{bi} - V_a), \quad (3)$$

where  $\epsilon$  is the permittivity of the material ( $\sim 8.6 \times 10^{-13}\ \text{F}/\text{cm}$  in 4H-SiC),  $N_{\text{eff}}$  is the position dependent effective carrier concentration, and  $V_{bi}$  is the built-in potential which is related to the barrier

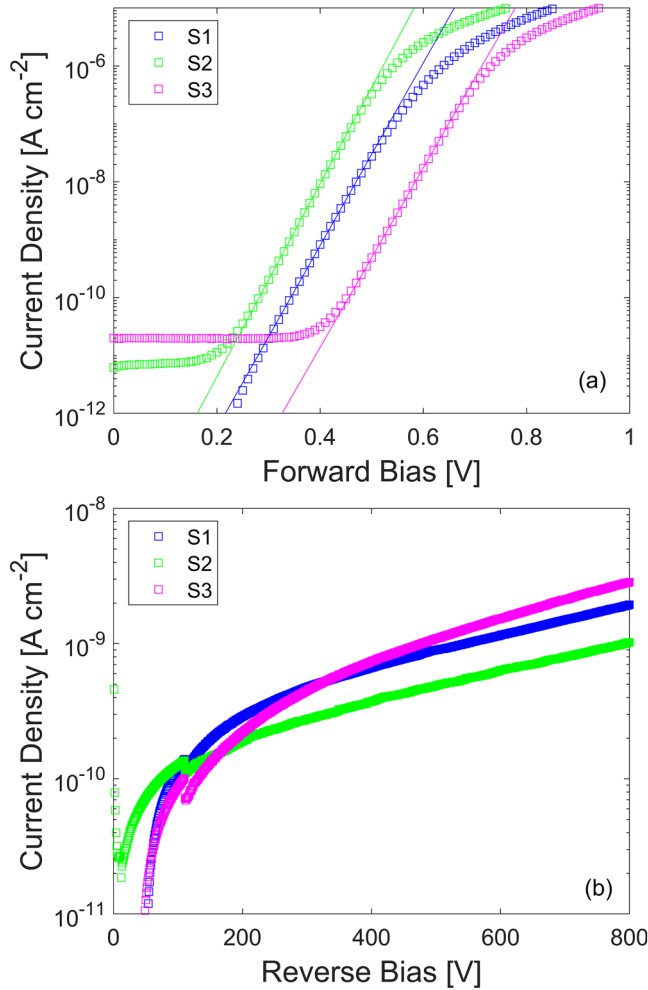


**FIG. 2.** Forward (a) and reverse (b) junction current plotted as a function of the applied bias for detectors S1, S2, and S3. The solid lines represent the straight line fit of the linear region.

height by Eq. (4),

$$\Phi_{B,C} = V_{bi} + k_B T \ln \frac{N_c}{N_{eff}}, \quad (4)$$

where  $N_c$  is the effective density of states of the conduction band which at room temperature is  $1.6 \times 10^{19} \text{ cm}^{-3}$ .<sup>41</sup> Figure 3(b) shows the Mott-Schottky plot for the detectors. A linear fit of the plots following Eq. (3) was used to calculate the effective carrier concentrations and were found to be  $9.8 \times 10^{13}$ ,  $1.8 \times 10^{14}$ , and  $1.7 \times 10^{14} \text{ cm}^{-3}$  for S1, S2, and S3, respectively. The nonlinear behavior of the Mott-Schottky plot of S1 indicates that the doping concentration is lower toward the surface of the device resulting in an unusually high effective built-in potential of 18.4 V. The Mott-Schottky plot suggests that for lower bias voltages, i.e., for a region

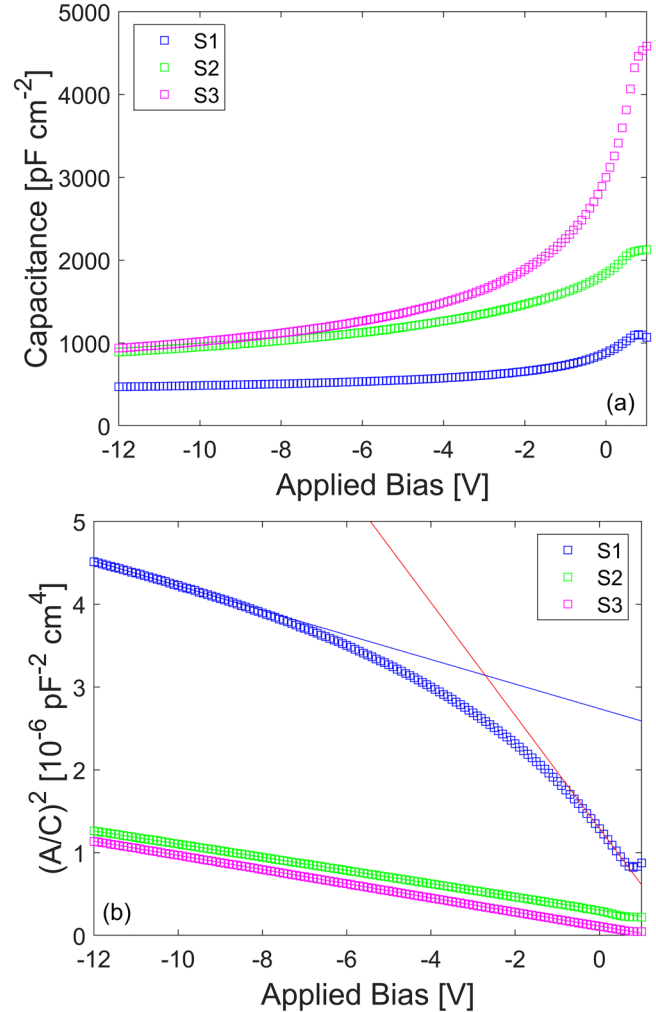


**FIG. 3.** The capacitance per unit area as a function of applied bias for the  $250 \mu\text{m}$  Ni/n-4H-SiC epitaxial radiation detectors (a) and the corresponding Mott-Schottky plots (b). The solid lines are the straight-line fits for calculating the effective doping concentration at two different bias regimes.

near the detector surface, the doping concentration is as low as  $2 \times 10^{13} \text{ cm}^{-3}$ . However, the same increased to  $9.8 \times 10^{13} \text{ cm}^{-3}$  when calculated in the higher bias region. The built-in potential calculated from the higher bias region was found to be 1.9 V which is more reasonable. The built-in potentials for S2 and S3 were calculated to be 3.9 and 1.3 V, respectively. Using Eq. (4), the barrier height is calculated to be 1.6 eV which is higher than that obtained from the forward  $I$ - $V$  characteristics due to the fact that the C- $V$  barrier height corresponding to the average barrier height over the entire region, whereas the  $I$ - $V$  barrier height represents the effective barrier height resulting from current preferring to pass through the low barrier portions of a spatially inhomogeneous barrier.<sup>42–44</sup> One of the challenges for  $250 \mu\text{m}$  epitaxial layer detectors is being able

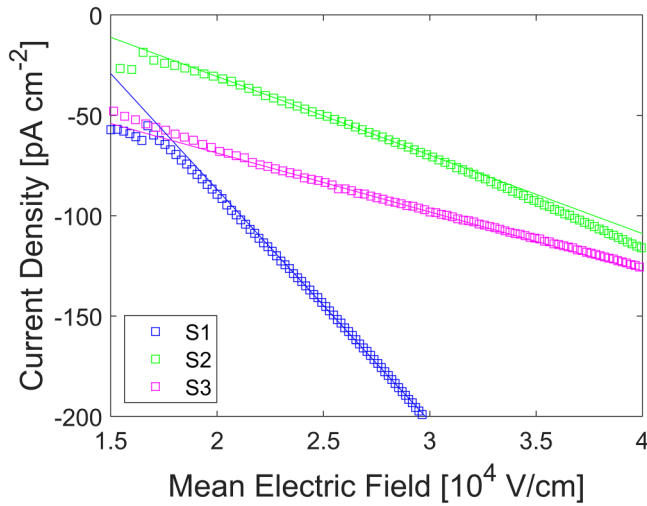


**FIG. 4.** Variation of current density under reverse bias as a function of mean electric field across the space charge region. The mean field can be converted to the maximum field at the interface by multiplying by 2. The solid lines are the straightline fits to the experimental data.

to fully deplete the space charge region without the device breaking down under the extremely high electric field. Based on the full depletion approximation to Poisson's equation, the maximum electric field at the interface of the detector is given by the following

$$E_m = \frac{qN_{eff}x_d}{\epsilon} \quad (5)$$

Using Eq. (5), at full depletion, the electric field strength at the metal–semiconductor interface would be 0.5, 0.9, and 0.8 MV/cm (5.7, 10.7, and 10.0 kV applied reverse bias) for S1, S2, and S3, respectively. Since the electric field strength is less than the breakdown field of silicon carbide ( $\sim 2.0$  MV/cm), the SBDs will be able to operate at full depletion without breaking down.

Based on a drift-diffusion model,<sup>41</sup> the diffusion current density  $J_{diff}$  due to electrons in the space charge region is given by

$$J_{diff} = q\mu_n E_m N_c \exp\left(-\frac{q\Phi_B}{k_B T}\right) \left[ \exp\left(-\frac{qV_R}{k_B T}\right) - 1 \right], \quad (6)$$

where  $\mu_n$  is the electron mobility which was assumed to be  $950 \text{ cm}^2/\text{Vs}$ ,<sup>45</sup>  $N_c$  is the effective density of states, and  $V_R$  is the applied reverse bias. At moderate electric field, the barrier lowering can be neglected making  $J_{diff}$  linear with the applied electric field. Figure 4 shows the  $J-E$  plot for the detectors at a moderate field strength ( $1-3 \times 10^4 \text{ V/cm}$ ) which is linear implying that the current is space-charge limited. From the slope of the linear fit, the barrier height was calculated to be  $\sim 1.1 \text{ eV}$  for all the three detectors. Based on thermionic emission-diffusion theory,<sup>39</sup> thermionic emission and diffusion occur in tandem with the slower of the two processes dominating. Under forward bias, it was assumed that thermionic

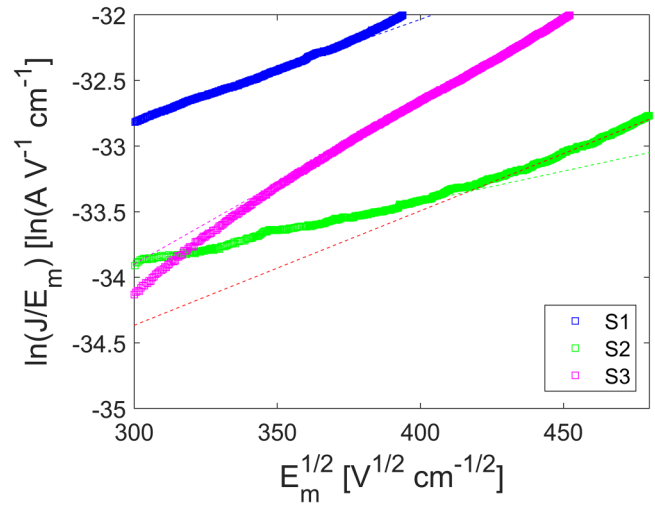


**FIG. 5.** Interfacial electric field dependence of the current density  $J$  normalized to the interfacial electric field  $E_m$ . Dashed lines are the linear fit of experimental data. S2 has a second linear fit in red corresponding to interfacial electric fields greater than  $0.2 \text{ MV/cm}$ .

emission was a current limiting process, thus explaining the discrepancy in calculated barrier height between forward and reverse bias. The difference could additionally be attributed to other space-charge limited current mechanisms such as carrier generation from defect levels. Generation–recombination depends linearly on the depletion width, which has a one-to-one correspondence to the electric field and is, therefore, indistinguishable from diffusion.<sup>37,38,46,47</sup> At high electric fields, the reduction in barrier due to the electric field becomes a significant factor and is given by Eq. (7) below,<sup>48</sup>

$$\Delta\Phi_B = \frac{1}{m} \sqrt{\frac{qE_m}{\pi\epsilon}} \quad (7)$$

Here,  $m$  is a scaling factor describing the barrier being reduced. For Schottky barrier lowering,  $m$  is equal to two. However, for detectors with significant charge carrier generation from defects in the space-charge region, Eq. (7) describes the Poole–Frenkel lowering of the trap barrier height instead and  $m$  is equal to one.<sup>10,49</sup> The dominant current mechanism between the two as a function of the interfacial electric field can then only be identified from the  $\ln J/E_m - E_m^{1/2}$  plot which is given in Fig. 5. From the slopes,  $m$  is calculated to be 1.2 for S1 and 0.8 for S3 indicating that the current at a high electric field is mostly trap-assisted. For S2,  $m$  is 2.0 up until  $\sim 2 \text{ MV/cm}$  at which point it drops to 1.1. This suggests that defects within the space-charge region have a weaker effect on the electrical properties for S2 than that in S1 and S3.

## B. Radiation detection measurements

Based on the drift-diffusion model,<sup>23</sup> full charge collection occurs when the depletion width is greater than or equal to the



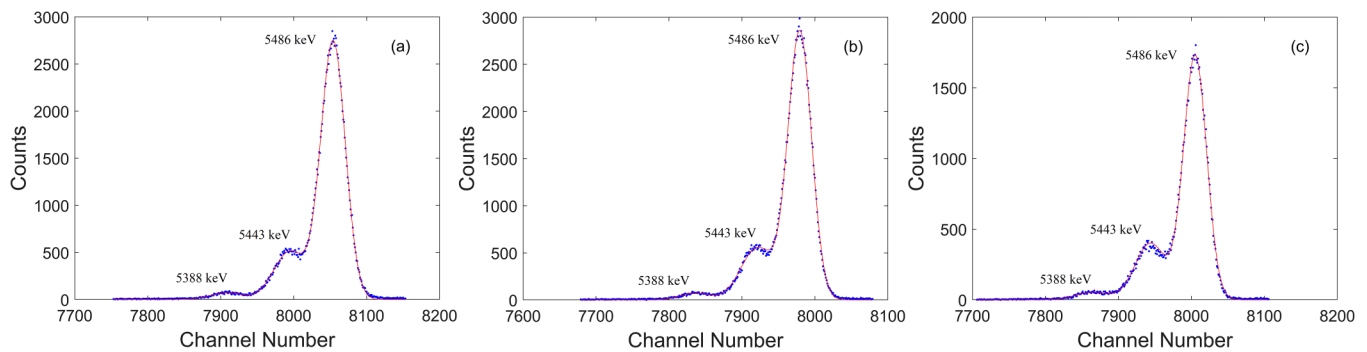


**FIG. 6.** Pulse height spectra obtained for the Ni/n-4H-SiC SBD S1 (a), S2 (b), and S3 (c) when exposed to a  $0.9\mu\text{Ci}^{241}\text{Am}$  source. The solid red lines are the triple gaussian model fitted overtop the PHS.

stopping range of incident charged ionizing particle. Based on SRIM<sup>50</sup> calculations, the range of  $5486\text{ keV}^{241}\text{Am}$  alpha particles in 4H-SiC is  $\sim 19\mu\text{m}$ . For all charges to be generated in the space charge region, reverse biases of 15 V for S1 or 60 V for S2 and S3 are required based on the full depletion approximation. Figure 6 shows the PHS obtained for the three radiation detectors at 200 V reverse bias, which is the optimum bias for the given conditions, while exposed to a  $^{241}\text{Am}$  alpha source. Energy resolutions of the detectors were calculated to be 0.49% (26.7 keV), 0.47% (25.6 keV), and 0.46% (25.1 keV) for S1, S2, and S3, respectively. In all three detectors, the 5388, 5443, and 5486 keV peaks corresponding to the three primary alpha emissions from the  $^{241}\text{Am}$  source were well resolved. Figure 7 shows the pulser peaks acquired using the same detection electronics, with and without the detector connected.

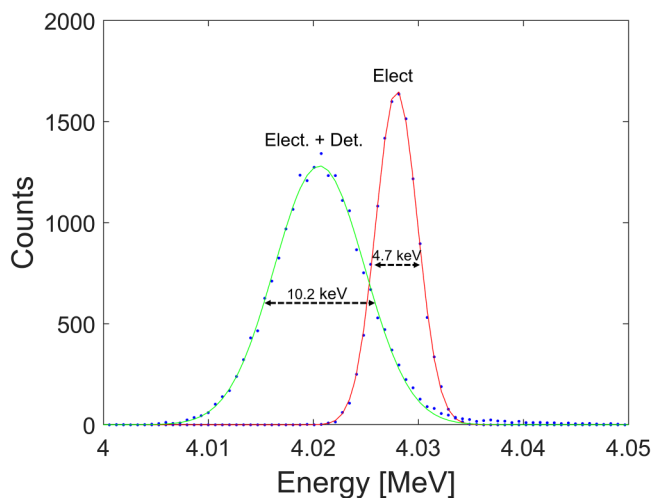


**FIG. 7.** Pulser PHS obtained using the spectrometer at an optimized setting with detector S3 connected and biased at  $-200\text{ V}$  (labeled Elect. + Det.) and without the detector connected (labeled Elect.). The shaping time used was  $1\mu\text{s}$ , and the pulser amplitude was kept identical in both the cases.

The noise is quantified as the FWHM of the pulser peaks ( $FWHM_{\text{pulser}}$ ). The  $FWHM_{\text{pulser}}$  was measured to be 10.2 keV with the detector connected which corresponds to the overall system noise consisting of the preamplifier, detector, and the interconnection between the two. Without the detector connected, the  $FWHM_{\text{pulser}}$  was 4.7 keV representing the open input preamplifier noise. The change in the  $FWHM_{\text{pulser}}$  indicates that detector capacitance is large compared to preamplifier input capacitance, which reduces the feedback loop gain of the preamplifier.

Figure 8 shows the CCE plotted against the reverse bias voltage for detector S1 using Eq. (1). At 200 V, the charge collection efficiencies for S1, S2, and S3 were calculated to be 99.6%, 98.4%, and 98.6%, respectively. Electrons and holes generated within the space-charge region are immediately swept toward the

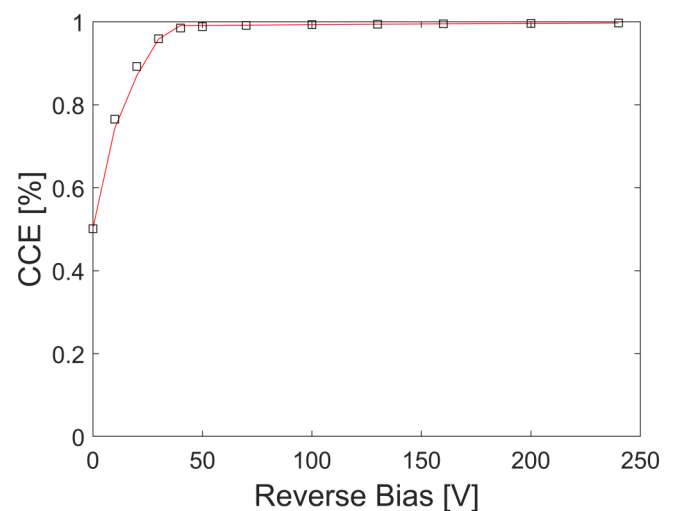


**FIG. 8.** Charge collection efficiency as a function of the applied reverse bias for detector S1. The solid red line corresponds to the drift-diffusion model for biases less than 40 V and the Hecht model for higher voltages.

bottom and top electrodes, respectively, by the strong internal electric field whereas charge carriers generated in the neutral region must first diffuse into the space charge region to be collected. This can be described numerically for a single charge type using the drift-diffusion model<sup>23</sup> given by

$$CCE = \frac{1}{E_a} \left\{ \int_0^{x_d} \left( \frac{dE}{dx} \right) dx + \int_{x_d}^{x_r} \left( \frac{dE}{dx} \right) \exp \left[ -\frac{x - x_d}{L_d} \right] dx \right\}, \quad (8)$$

where  $dE/dx$  is the stopping power of the alpha particle,  $x_r$  is the range of the particle, and  $L_d$  is the minority carrier diffusion length. Fitting the drift-diffusion region of the curve to Eq. (8), the best fit to the data occurs with a built-in voltage of  $\sim 2$  V and minority carrier diffusion length of  $\sim 10 \mu\text{m}$ . Within the saturation region of the CCE vs applied reverse bias curve, all carriers will drift and thus will follow the Hecht equation.<sup>51,52</sup> For electrons, the internal field is high enough to force electrons to saturation velocity. Thus, the drift velocity of electrons stays constant, while transit distance keeps expanding with increased bias putting subtle downward pressure on the CCE curve. Meanwhile, due to their lower mobility, the hole drift velocity will remain proportional to the mean internal electric field. Since the transit distance remains constant for holes, this puts upward pressure on the CCE curve at least until the hole velocity finally saturates. This is summarized in Eq. (9),

$$CCE_{elect} = \frac{\lambda_e}{x_d} \left[ 1 - \exp \left( -\frac{x_d}{\lambda_e} \right) \right], \quad (9a)$$

$$CCE_{holes} = \frac{E}{\lambda_h} \left[ 1 - \exp \left( -\frac{\lambda_h}{E} \right) \right]. \quad (9b)$$

Here,  $\lambda_e$  and  $\lambda_h$  are arbitrary fitting constants. Thus, a possible explanation for the difference in charge collection efficiency between the three detectors could be that holes in S2 and S3 have reached saturation velocity due to the higher electric field strength at the same bias compared to S1 leaving only downward pressure on the CCE. Applying both models given in Eqs. (8) and (9) to Fig. 8 results in a mean absolute percent error of 0.54%. The above results obtained from the  $I$ - $V$ ,  $C$ - $V$ , and the radiation detection measurements are summarized in Table I.

### C. Defect characterization

DLTS measurements were performed on detector S3 at a steady-state reverse bias of 2 V. This pushes the fermi-level below the trap-levels within the depletion region making the trap levels prefer to empty themselves electronically. Every 1000 ms, a 0 V

filling pulse was applied for  $1 \mu\text{s}$ , pushing the fermi-level above the trap levels for a region  $\Delta x$ . For S3,  $\Delta x$  was  $1.7 \mu\text{m}$ . After the filling pulse ends, the fermi-level returns to its steady-state position as the traps within  $\Delta x$  start to empty at a rate defined by the Arrhenius equations given in Eq. (10) below,<sup>53</sup>

$$e_n = \sigma_n \beta T^2 \exp \left( \frac{-E_a}{k_B T} \right). \quad (10)$$

Here,  $\sigma_n$  is the trap's electron capture cross section and  $\beta$  is a constant such that  $\beta T^2$  is equal to the product of the effective density of states of the conduction band and the mean thermal velocity. For 4H-SiC,  $\beta$  is taken to be  $\sim 3.0 \times 10^{21} \text{ cm}^{-2} \text{ K}^{-2} \text{ s}^{-1}$ . Finally,  $E_a$  is the activation energy of trap measured relative to the conduction band minimum. As the electrons thermally emit, the net positive charge within the depletion region increases back to its steady-state value, resulting in a time-dependent capacitance given by

$$C(t) = C_{ss} + \Delta C \exp(-te_n), \quad (11)$$

where  $C_{ss}$  is the steady-state capacitance at the applied reverse bias and  $\Delta C$  is the additional capacitance from the trapped electrons just prior to emission. Figure 9(a) shows the DLTS spectra for detector S3 for six correlators from 0.05 to 50 ms over the temperature range of 80–790 K which showed three discernable peaks. The corresponding Arrhenius plots of these peaks are shown in Fig. 9(b). For trap concentrations  $N_t \ll N_{eff}$ ,  $N_t$  can be calculated from the following equation:

$$N_t = 2 \left( \frac{\Delta C}{C_{ss}} \right) N_{eff}. \quad (12)$$

$\Delta C$  is taken to be the average of the magnitudes of the DLTS peaks of the same type divided by the normalized DLTS signal maximum which is 0.55 for the DDS-12's rate window. The trap parameters obtained from the peaks in the DLTS spectra are given in Table II.

All three trap centers had concentration of the order of  $10^{11} \text{ cm}^{-3}$  and capture cross sections of the order of  $10^{-15} \text{ cm}^2$ . The trap center  $T_1$  at 0.16 eV is attributed to ionized titanium in the cubic (c) Si lattice site and is designated as Ti (c).<sup>54–57</sup> The concentration is one order of magnitude lower than what has been reported for our recent 50 and  $150 \mu\text{m}$ <sup>10,57</sup> detectors while the cross section was one and two orders of magnitude lower than the 50 and  $150 \mu\text{m}$  detectors, respectively. For a trap with a spherical volume, the cross section can be related to an effective trap radius  $r_{tr}$  by Eq. (13),

$$\sigma_n = \pi r_{tr}^2. \quad (13)$$

**TABLE I.** Electrical and spectroscopic parameters obtained for the three SBDs fabricated on  $250 \mu\text{m}$  epitaxial layers.

Detector ID	Ideality factor	$\Phi_B$ (eV)	Leakage current density @ $-800$ V (nA $\text{cm}^{-2}$ )	$N_{eff}$ ( $10^{14} \text{ cm}^{-3}$ )	Shaping time ( $\mu\text{s}$ )	Energy resolution (%)	CCE @ $-200$ V (%)
S1	1.06	1.35	1.9	0.97	3	0.49	99.6
S2	1.00	1.31	1.0	1.8	2	0.48	98.4
S3	1.08	1.45	2.9	1.7	1	0.47	98.6

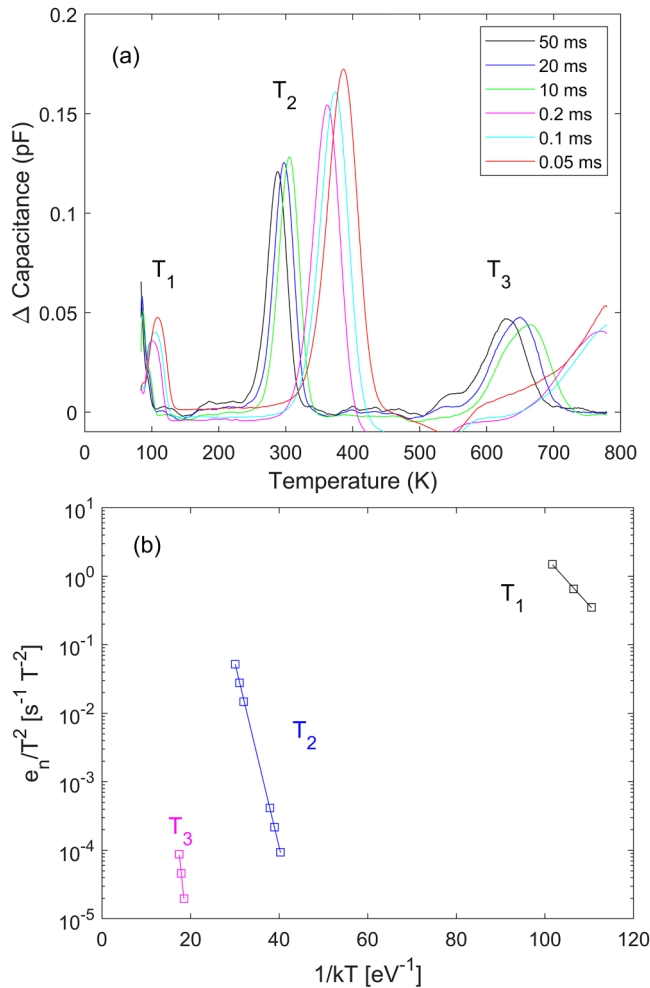


**FIG. 9.** DLTS spectra obtained for Ni/n-4H-SiC Schottky barrier detector S3 in the temperature range of 80–790 K for six correlators with initial delays 0.05–50 ms (a) and the Arrhenius plots corresponding to the three DLTS peaks (the solid lines are the linear fit) (b).

For cross sections on the order of  $10^{-15} \text{ cm}^2$ , effective radii are  $\sim 2\text{--}5 \text{ \AA}$  which is the same order of magnitude as bond lengths and lattice constants. This suggests that the Ti impurities are on average point like, and therefore Ti clustering must be reduced compared to

**TABLE II.** Trap parameters obtained from the DLTS measurements of Schottky barrier detector S3.

Peak	$E_c - E_T$ (eV)	$\sigma_n$ ( $10^{-15} \text{ cm}^2$ )	$N_t$ ( $10^{11} \text{ cm}^{-3}$ )	Possible trap identity
T <sub>1</sub>	0.16	7.18	2.90	Ti (c)
T <sub>2</sub>	0.62	1.78	8.61	Z <sub>1/2</sub>
T <sub>3</sub>	1.43	1.63	2.58	EH <sub>6/7</sub>

many of our thinner epilayer detectors.<sup>10,40,57</sup> The trap centers T<sub>2</sub> at 0.62 eV and T<sub>3</sub> at 1.43 eV are well established to be Z<sub>1/2</sub> and EH<sub>6/7</sub>, respectively, and appear in almost all 4H-SiC devices.<sup>56,58,59</sup> The two defect centers are correlated and attributed to the neutral and doubly positive charge states of the carbon vacancy, respectively.<sup>60–62</sup> As with T<sub>1</sub>, the small cross sections of  $\sim 10^{-15} \text{ cm}^2$  indicate that they are on average single atom related rather than clusters. How significantly individual trap centers affect device performance is related to the trap's attenuation constant which is the product of the capture cross section and trap concentration. Compared to our 20  $\mu\text{m}$  epitaxial layer detector (AS2) with a 0.38% resolution, the trap concentration of Z<sub>1/2</sub> is an order of magnitude lower while the capture cross section is a magnitude higher.<sup>63</sup> This makes the attenuation constant of the same order of magnitude. For EH<sub>6/7</sub>, the trap concentration in the present detector is an order of magnitude lower with approximately the same cross section compared to AS2.

#### IV. CONCLUSIONS

Ni/n-4H-SiC Schottky barrier detectors have been fabricated on the 250  $\mu\text{m}$  epitaxial layers, thickest ever reported for radiation detection. The present study on 250  $\mu\text{m}$  Ni/4H-SiC SBDs represents a quantum step in the development of radiation monitoring systems for harsh environments. Traditional high-Z semiconductor radiation detectors such as HPGe or CdZnTe are inoperable in harsh environments with high temperature or high radiation background. This necessitates the use of harsh environments ready semiconductors such as 4H-SiC. The large thickness of 250  $\mu\text{m}$  opens the possibility for the collection of penetrating radiations such as x- and gamma rays as well.

Due to the low effective doping concentrations of  $< 2 \times 10^{14} \text{ cm}^{-3}$  and high barrier heights of  $> 1.3 \text{ eV}$ , the reverse bias leakage current was found to be space-charge limited. Analysis regarding the barrier lowering of the space-charge limited current from the  $\ln J/E_m - E_m^{1/2}$  plot revealed that for the detectors with ideality factors of  $> 1.05$ , the barrier lowering was due to the Poole-Frenkel effect indicating that the current was trap assisted. However, the detector with the ideality factor of 1.00 showed Schottky barrier lowering up to 2 MV/cm of applied electric field before transitioning to the Poole-Frenkel effect indicating that the influence of traps was weaker than the other samples. Exposing the detectors with a <sup>241</sup>Am alpha source showed an energy resolution in the PHS of less than 0.5% for all three detectors at  $-200 \text{ V}$ . The charge collection efficiencies were measured to be 98%–99% with no correlation to the energy resolutions. A drift-diffusion model fit to the variation of CCE as a function of bias voltage revealed a minority carrier diffusion length of  $\sim 10 \mu\text{m}$ . Additionally, due to the low doping concentration, all the detectors can operate at full depletion without breaking down which is a key limitation for ultra-thick radiation detectors. Further investigations are under way to study the behavior of the detectors at full-depletion bias voltage.

To investigate how defects inhibit the detectors performance, the detector which exhibited the best resolution was characterized by capacitance-DLTS from 80 to 790 K. Three peaks were observed corresponding to Ti(c), Z<sub>1/2</sub>, and EH<sub>6/7</sub>. All the three defects had low concentrations on the order of  $10^{11} \text{ cm}^{-3}$  and small capture cross sections of  $10^{-15} \text{ cm}^2$  indicating that defects are mostly single



atom related rather than clusters. Comparing with the case of our previously fabricated detectors, it can be inferred that the pulse height peak widening cannot solely be attributed to defects in the epilayer. In fact, the resolution of S3 being higher than S2 hints that performance is related to the total leakage current, which is smaller for S3 than the other detectors due to its smaller contact area. Taking this into account, the resolution could be improved by reducing the leakage current through surface passivation.

## AUTHORS' CONTRIBUTIONS

All authors contributed equally to this work.

## ACKNOWLEDGMENTS

This work was supported by the DOE Office of Nuclear Energy's Nuclear Energy University Program (NEUP), Grant Nos. DE-AC07-051D14517 and DE-NE0008662. The work was also supported in part by the Advanced Support Program for Innovative Research Excellence-I (ASPIRE-I), Grant No. 15530-E404 and Support to Promote Advancement of Research and Creativity (SPARC), Grant No. 15530-E422 of the University of South Carolina (UofSC), Columbia, USA.

## DATA AVAILABILITY

The data that support the findings of this study are available from the corresponding author upon reasonable request.

## REFERENCES

- <sup>1</sup>N. R. Taylor, Y. Yu, M. Ji, T. Aytug, S. Mahurin, R. Mayes, S. Cetiner, M. Paras Paranthaman, D. Ezell, L. R. Cao, and P. C. Joshi, *Appl. Phys. Lett.* **116**, 252108 (2020).
- <sup>2</sup>V. V. Kozlovski, A. A. Lebedev, M. E. Levinshtein, S. L. Rumyantsev, and J. W. Palmour, *J. Appl. Phys.* **123**, 024502 (2018).
- <sup>3</sup>G. Bertuccio, D. Puglisi, L. Torrisi, and C. Lanzieri, *Appl. Surf. Sci.* **272**, 128 (2013).
- <sup>4</sup>F. Zhao, M. M. Islam, and C.-F. Huang, *Mater. Lett.* **65**, 409 (2011).
- <sup>5</sup>L. F. Voss, C. D. Frye, M. Bora, D. L. Hall, P. V. Grivickas, and A. Conway, *J. Vac. Sci. Technol. B* **37**, 040601 (2019).
- <sup>6</sup>J. Pernot, W. Zawadzki, S. Contreras, J. L. Robert, E. Neyret, and L. Di Cioccio, *J. Appl. Phys.* **90**, 1869 (2001).
- <sup>7</sup>S. O. Kasap, M. Z. Kabir, K. O. Ramaswami, R. E. Johanson, and R. J. Curry, *J. Appl. Phys.* **128**, 124501 (2020).
- <sup>8</sup>M. Zahangir Kabir, E. V. Emelianova, V. I. Arkhipov, M. Yunus, S. O. Kasap, and G. Adriaenssens, *J. Appl. Phys.* **99**, 124501 (2006).
- <sup>9</sup>F. H. Ruddy, J. G. Seidel, H. Chen, A. R. Dulloo, and S.-H. Ryu, *IEEE Trans. Nucl. Sci.* **53**, 1713 (2006).
- <sup>10</sup>S. K. Chaudhuri, J. W. Kleppinger, and K. C. Mandal, *J. Appl. Phys.* **128**, 114501 (2020).
- <sup>11</sup>D. Puglisi and G. Bertuccio, *Micromachines* **10**, 835 (2019).
- <sup>12</sup>C. S. Bodie, G. Lioliou, and A. M. Barnett, *Nucl. Instrum. Meth. Phys. Res. A* **985**, 164663 (2021).
- <sup>13</sup>M. Hodgson, A. Lohstroh, P. Sellin, and D. Thomas, *Meas. Sci. Technol.* **28**, 105501 (2017).
- <sup>14</sup>P. G. Neudeck, D. J. Spry, M. J. Krasowski, N. F. Prokop, and L. Chen, *Mater. Sci. Forum* **963**, 813 (2019).
- <sup>15</sup>G. Lucas and L. Pizzagalli, *Nucl. Instrum. Meth. Phys. Res. B* **229**, 359 (2005).
- <sup>16</sup>L. Torrisi, G. Foti, L. Giuffrida, D. Puglisi, J. Wolowski, J. Badziak, P. Parys, M. Rosinski, D. Margarone, and J. Krasa, *J. Appl. Phys.* **105**, 123304 (2009).
- <sup>17</sup>X. Zhang, J. W. Cates, J. P. Hayward, G. Bertuccio, D. Puglisi, and P. A. Hausladen, *IEEE Trans. Nucl. Sci.* **60**, 2352–2356 (2013).
- <sup>18</sup>G. Bertuccio, D. Puglisi, L. Torrisi, and C. Lanzieri, *Appl. Surf. Sci.* **272**, 128 (2013).
- <sup>19</sup>S. M. Griffin, Y. Hochberg, K. Inzani, N. Kurinsky, T. Lin, and T. C. Yu, *Phys. Rev. D* **103**, 075002-1-29 (2021).
- <sup>20</sup>J. Wu, Y. Jiang, M. Li, L. Zeng, J. Li, H. Gao, D. Zou, Z. Bai, C. Ye, W. Liang, S. Dai, Y. Lu, R. Rong, J. Du, and X. Fan, *Rev. Sci. Instrum.* **88**, 083301 (2017).
- <sup>21</sup>Z. Wang, D. Zhou, W. Xu, D. Pan, F. Ren, D. Chen, R. Zhang, Y. Zheng, and H. Lu, *IEEE Photonic Tech. Lett.* **32**, 791 (2020).
- <sup>22</sup>B. Zat'ko, F. Dubecký, A. Šagátová, K. Sedláčková, and L. Ryč, *J. Instrum.* **10**, C04009 (2015).
- <sup>23</sup>S. K. Chaudhuri, K. J. Zavalla, and K. C. Mandal, *Nucl. Instrum. Meth. Phys. Res. A* **728**, 97 (2013).
- <sup>24</sup>G. Bertuccio, R. Casiraghi, and F. Nava, *IEEE Trans. Nucl. Sci.* **48**, 232 (2001).
- <sup>25</sup>G. Lioliou, N. R. Gemmell, M. Mazzillo, A. Sciuto, and A. M. Barnett, *Nucl. Instrum. Meth. Phys. Res. A* **940**, 328 (2019).
- <sup>26</sup>G. Lioliou, H. K. Chan, T. Gohil, K. V. Vassilevski, N. G. Wright, A. B. Horsfall, and A. M. Barnett, *Nucl. Instrum. Method Phys. Res. A* **840**, 145 (2016).
- <sup>27</sup>K. C. Mandal, P. G. Muzykov, S. K. Chaudhuri, and J. R. Terry, *IEEE Trans. Nucl. Sci.* **60**, 2888 (2013).
- <sup>28</sup>K. C. Mandal, P. G. Muzykov, and J. Russell Terry, *Appl. Phys. Lett.* **101**, 051111 (2012).
- <sup>29</sup>W. Cunningham, A. Gouldwell, G. Lamb, J. Scott, K. Mathieson, P. Roy, R. Bates, P. Thornton, K. M. Smith, R. Cusco, M. Glaser, and M. Rahman, *Nucl. Instrum. Meth. Sci. Res. A* **487**, 33–39 (2002).
- <sup>30</sup>F. Ruddy, J. G. Seidel, R. W. Flammang, R. Singh, and J. Schroeder, in *IEEE Nuclear Science Symposium Conference Record, R15-4, 19–25 Oct. 2008* (IEEE, 2008), pp. 449–455.
- <sup>31</sup>G. Bertuccio, D. Puglisi, A. Pullia, and C. Lanzieri, *IEEE Trans. Nucl. Sci.* **60**, 1436–1441 (2013).
- <sup>32</sup>Q. Wahab, A. Ellison, A. Henry, and E. Janzén, *Appl. Phys. Lett.* **76**, 2725 (2000).
- <sup>33</sup>R. Yakimova, N. Vouroutzis, M. Syväjärvi, and J. Stoemenos, *J. Appl. Phys.* **98**, 034905 (2005).
- <sup>34</sup>P. G. Neudeck, *Mater. Sci. Forum* **338-342**, 1161 (2000).
- <sup>35</sup>W. Kern, *J. Electrochem. Soc.* **137**, 1887 (1990).
- <sup>36</sup>S. K. Chaudhuri, K. J. Zavalla, and K. C. Mandal, *Appl. Phys. Lett.* **102**, 031109 (2013).
- <sup>37</sup>E. H. Rhoderick, *IEE Proc. I Solid State Electron. Dev.* **129**, 1 (1982).
- <sup>38</sup>L. Changshi, *ECS J. Solid State Sci. Technol.* **9**, 064007 (2020).
- <sup>39</sup>S. M. Sze and K. K. Ng, *Physics of Semiconductor Devices* (John Wiley & Sons, New York, 2007).
- <sup>40</sup>K. V. Nguyen, M. A. Mannan, and K. C. Mandal, *IEEE Trans. Nucl. Sci.* **62**, 3199 (2015).
- <sup>41</sup>M. E. Levinshtein, S. L. Rumyantsev, and M. Shur, *Properties of Advanced Semiconductor Materials: GaN, AlN, InN, BN, SiC, SiGe* (Wiley, New York, 2001).
- <sup>42</sup>R. T. Tung, *Phys. Rev. B* **45**, 13509 (1992).
- <sup>43</sup>M. Jun, M. Jang, Y. Kim, C. Choi, T. Kim, S. Oh, and S. Lee, *J. Vac. Sci. Technol. B* **26**, 137 (2008).
- <sup>44</sup>G. Baccarani, *J. Appl. Phys.* **47**, 4122 (1976).
- <sup>45</sup>P. A. Ivanov, A. S. Potapov, T. P. Samsonova, and I. V. Grekhov, *Solid State Electron.* **123**, 15 (2016).
- <sup>46</sup>W. Shockley and W. T. Read, *Phys. Rev.* **87**, 835 (1952).
- <sup>47</sup>R. N. Hall, *Phys. Rev.* **87**, 387 (1952).
- <sup>48</sup>S. M. Sze and M. K. Lee, *Semiconductor Devices: Physics and Technology* (Wiley, Singapore, 2013).
- <sup>49</sup>H. Schroeder, *J. Appl. Phys.* **117**, 215103 (2015).
- <sup>50</sup>J. F. Ziegler, M. D. Ziegler, and J. P. Biersack, *Nucl. Instrum. Meth. Phys. Res. B* **268**, 1818 (2010).
- <sup>51</sup>K. Hecht, *Z. Phys.* **77**, 235 (1932).
- <sup>52</sup>V. Radeka, *Ann. Rev. Nucl. Part. Sci.* **38**, 217 (1988).
- <sup>53</sup>D. V. Lang, *J. Appl. Phys.* **45**, 3023 (1974).

- <sup>54</sup>T. Dalibor, G. Pensl, N. Nordell, and A. Schöner, *Phys. Rev. B* **55**, 13618 (1997).
- <sup>55</sup>Ł. Gelczuk, M. Dąbrowska-Szata, M. Sochacki, and J. Szmids, *Solid State Electron.* **94**, 56 (2014).
- <sup>56</sup>J. Zhang, L. Storasta, J. P. Bergman, N. T. Son, and E. Janzén, *J. Appl. Phys.* **93**, 4708 (2003).
- <sup>57</sup>J. W. Kleppinger, S. K. Chaudhuri, and K. C. Mandal, *Proc. SPIE* **11494**, 11490X (2020).
- <sup>58</sup>G. Alfieri and T. Kimoto, *Appl. Phys. Lett.* **102**, 152108 (2013).
- <sup>59</sup>K. Danno, T. Kimoto, and H. Matsunami, *Appl. Phys. Lett.* **86**, 122104 (2005).
- <sup>60</sup>L. Gordon, A. Janotti, and C. G. Van de Walle, *Phys. Rev. B* **92**, 045208 (2015).
- <sup>61</sup>T. Kobayashi, K. Harada, Y. Kumagai, F. Oba, and Y.-I. Matsushita, *J. Appl. Phys.* **125**, 125701 (2019).
- <sup>62</sup>X. Yan, P. Li, L. Kang, S.-H. Wei, and B. Huang, *J. Appl. Phys.* **127**, 085702 (2020).
- <sup>63</sup>K. C. Mandal, S. K. Chaudhuri, K. V. Nguyen, and M. A. Mannan, *IEEE Trans. Nucl. Sci.* **61**, 2338 (2014).